INSTITUTE OF PHYSICS PUBLISHING MODELLING AND SIMULATION IN MATERIALS SCIENCE AND ENGINEERING

Modelling Simul. Mater. Sci. Eng. **14** (2006) 1211–1223 doi:10.1088/0965-0393/14/7/009

Finite element simulations of microvoid growth due to selective oxidation in binary alloys

S Pal and D V Kubair

Computational Dynamic Fracture Mechanics Laboratory, Department of Aerospace Engineering, Indian Institute of Science, Bangalore-560012

E-mail: kubair@aero.iisc.ernet.in

Received 28 April 2006, in final form 21 August 2006
Published 26 September 2006
Online at stacks.iop.org/MSMSE/14/1211

Abstract

Selective oxidation induced void growth is observed in thermal barrier coating systems used in gas turbines. These voids occur at the interface between the bond coat (BC) and the thermally grown oxide (TGO) layer. In this paper we develop the modelling framework to simulate microvoid growth due to coupled diffusion and creeping in binary alloys. We have implemented the modelling framework into an existing finite element programme. The developed modelling framework and programme is used to simulate microvoid growth driven by selective oxidation in a binary β-NiAl alloy. Axisymmetric void growth due to the combined action of interdiffusion and creeping is simulated. The sharpness of the void and direction of creeping are considered as parameters in our study. Our simulations show that the voids dilate without any change in shape when creeping is equally likely in all the directions (isotropic). Void growth patterns similar to those observed in experiments are predicted when the creeping is restricted to occur only along the radial and tangential directions. A hemispherical void grows faster compared to a sharp void. The sharpness increases in the case of a sharp void and could lead to interactions with the neighbouring voids leading to spallation of the TGO layer as observed in experiments.

(Some figures in this article are in colour only in the electronic version)

1. Introduction

Thermal barrier coatings (TBCs) are used in gas turbine engines to increase their thermal efficiency by allowing an increase in the inlet gas temperature. These coatings are typically made of a columnar ceramic layer that provides thermal insulation. A sacrificial metallic bond coat (BC) layer, typically made of MCrAlY (where M is a metal namely Ni, Co, Fe or other combinations) is deposited above the superalloy substrate and below the TBC. The TBC provides insulation from high temperature, but is transparent to the flow of

oxygen and hence, the underlying BC layer is susceptible to oxidation induced failure. There are several studies both experimental and modelling that have addressed the issue of failure of the TBC systems. The commonly observed failure mechanisms are BC rumpling (Karlsson and Hutchinson 2002) and ratcheting induced cracking (Evans *et al* 2001, Xu *et al* 2003). Rumpling of the TGO has also been observed during cyclic oxidation leading to spallation of the TBC layer (Tolpygo and Clarke 2000, 2004a, 2004b, Balint and Hutchinson 2005). The above mentioned spallation was described to be due to the oxidation induced voids in the BC layer (Tolpygo and Clarke 2003). In a recent article, Suo *et al* (2003) developed a framework to model the stresses generated due to the action of non-reciprocal diffusion (Kirkendall effect). The so-developed framework was used to model the selective oxidation in a semi-infinite binary alloy system. In their 1D analysis void nucleation and growth was not considered. However, their analysis indicated that a tensile mean stress is generated near the interface in a Ni rich alloy. When the generated mean tensile stress is of sufficient magnitude voids could nucleate as observed in oxidation experiments (Provenzano *et al* 1988, Brumm and Grabke 1993, Liu and Gao 2000, Svensson *et al* 2003, Zimmermann *et al* 2003). During oxidation of NiAl, aluminium is depleted at the metal oxide interface leading to a concentration gradient and thereby diffusing aluminium from the bulk alloy to the interface. When a nickel rich NiAl is oxidized, Al gets depleted at the interface and Ni diffuses into the bulk to compensate for the material loss. In such a scenario Ni diffuses faster into the alloy than Al diffusing out (Shankar and Siegle 1978) causing a non-reciprocal diffusion leading to an unbalanced dilatational field, which is accommodated by the creeping of the surrounding metal. In the present paper we simulate the microvoid growth due to the above mentioned non-reciprocal diffusion.

There are several numerical studies available in the literature that have addressed the stresses generated and void growth due to diffusion. Needleman and Rice (1980) studied the growth of cavities along the grain interface due to grain boundary diffusion. Suo (2004) has formulated a continuum theory coupling creep and diffusion in pure metals. In the present study, we have extended the modelling framework developed by Suo *et al* (2003) to a general 3D setting, particularly to an axisymmetric scenario. This developed modelling framework is implemented into an existing finite element scheme, which is used to model the growth of a microvoid driven by coupled diffusion and creeping in a binary alloy. The details of the derivation of the axisymmetric modelling and the finite element scheme are presented in section 2. In section 3, we have described the boundary value problem pertaining to the selective oxidation of NiAl. The results obtained from varying the sharpness of the void and the creeping behaviour are discussed in section 4.

2. Axisymmetric formulation

In a recent paper by Suo *et al* (2003), the one-dimensional formulation of the coupled diffusion and creeping in binary alloys was described. Their formulation was used to analyse a 1D selective oxidation process in β-NiAl. Their analysis showed that, a large magnitude tensile stress is generated due to the selective oxidation of aluminium. Such large magnitude tensile stresses could lead to the nucleation of voids in a binary alloy. In the present paper we aim at simulating the growth of a microvoid thus created and subjected to further action of the coupled diffusion and creeping. As a first step we extend the 1D formulation of Suo *et al* (2003) to 3D. The 3D framework is used to analyse the axisymmetric microvoid growth problem in a binary alloy of metals A–B. In our formulation we assume that material A diffuses out of the continuum to form an oxide $A_{\mathrm{n}}O_{\mathrm{m}}$. The axisymmetric domain considered in the present analysis is defined in the r–z coordinates as shown in figure 2, with r being the radius vector and

z being coincident with the axis of revolution. The static stress equilibrium for the axisymmetric case can be written as

$$\frac{1}{r}\frac{\partial(rs_{rr})}{\partial r} - \frac{s_{\theta\theta}}{r} + \frac{\partial s_{rz}}{\partial z} + \frac{\partial p}{\partial r} = 0, \tag{1a}$$

$$\frac{1}{r}\frac{\partial(rs_{zr})}{\partial r} + \frac{\partial s_{zz}}{\partial z} + \frac{\partial p}{\partial z} = 0. \tag{1b}$$

In the equation above, s is the deviatoric stress. The deviatoric stress tensor (s) is related to the stress tensor (σ) and hydrostatic pressure (p) as $s = \sigma - pI$, with I being the identity matrix. For an axisymmetric problem the hydrostatic pressure p is defined as

$$p = (\sigma_{rr} + \sigma_{\theta\theta} + \sigma_{zz})/3. \tag{2}$$

In our formulation we assume that the total strain-rate ($\dot{\epsilon}$) to be infinitesimally small and hence can be additively decomposed into the creep strain rate ($\dot{\epsilon}^c$) and diffusional strain rate ($\dot{\epsilon}^d$). The total strain rate can be written as

$$\dot{\epsilon} = \dot{\epsilon}^c + \dot{\epsilon}^d = \tfrac{1}{2}(\nabla v + \nabla v^T), \tag{3}$$

where v is the particle velocity in the continuum. As described in Suo *et al* (2003) the differential diffusion (Kirkendall effect) of the elements of a binary alloy gives rise to the diffusional strain rate and is related to the gradient of the mass flux as

$$\dot{\epsilon}^d = \beta\nabla \cdot v = -\beta\Omega\nabla \cdot J, \tag{4}$$

where β is the diagonal matrix describing the preferential placement of the atoms along the r, θ or z directions, respectively. The diffusion flux J introduced in equation (4) is related to both the concentration and hydrostatic-pressure gradients as

$$J = -\frac{\Delta}{\Omega}\nabla c + \frac{\bar{D}}{\phi\kappa T}\nabla p, \tag{5}$$

where $\bar{D} = cD^A + (1-c)D^B$ is the average diffusivity, $\Delta = D^A - D^B$ is the differential diffusivity, ϕ is the Darken's thermodynamic factor, Ω is the atomic volume, κ is the Boltzmann constant and T is the absolute isothermal temperature of the continuum. In the definition of the average diffusivity ($\bar{D}$) and differential diffusivity (Δ), D^A and D^B correspond to the individual intrinsic diffusivities of the atoms A and B, respectively. For example, in the case of β-NiAl considered in the present study, B = Ni while A = Al as aluminium diffuses out and forms an oxide (Al_2O_3) . As described in Suo *et al* (2003), the diffusional flux will have a contribution from the concentration gradient only when $D^A \neq D^B$ (Kirkendall effect). In the present formulation we have assumed the inelastic (creep) deformation to follow J_2-flow theory and hence the creep deformation is isochoric (volume preserving), which leads to the continuity equation given by

$$\nabla \cdot v = \nabla \cdot \left[\Delta\nabla c - \frac{\bar{D}\Omega}{\phi\kappa T}\nabla p\right]. \tag{6}$$

The concentration evolution of the A atoms can be written as

$$\frac{\partial c}{\partial t} - \nabla \cdot \left[(D^A\nabla c) - cv - \left(\frac{cD^A\Omega}{\phi\kappa T}\nabla p\right)\right] = 0, \tag{7}$$

where c is the non-dimensional concentration of A atoms. In our analysis we have allowed the intrinsic diffusivities D^A and D^B to be functions of the current concentration $c(t)$, which are expressed as an expansion about the initial concentration c_o.

Following the analysis of Suo *et al* (2003) we introduce scaling parameters, which are then used to non-dimensionalize the governing differential equations. The stress components scale with Σ, which is related to the specific thermal energy as

$$\Sigma = \frac{\phi\kappa T}{\Omega}. \tag{8}$$

Using the equation above, the reference stress σ_o can be normalized as

$$\Theta = \frac{\sigma_0\Omega}{\phi\kappa T} = \frac{\sigma_0}{\Sigma}. \tag{9}$$

The coupled diffusion and creep problem has a characteristic (or natural) length scale, denoted here as Λ, which is related to the normalized reference stress Θ, reference strain-rate $\dot{\epsilon}_o$ and the interdiffusion coefficient at c_o, that is $D_o = (1 - c_o)D^A + c_o D^B$. The length scale is given by

$$\Lambda = \sqrt{\frac{D_0\Theta}{\dot{\epsilon}_0}}. \tag{10}$$

The particle velocity is scaled by $\dot{\epsilon}\Lambda/\Theta$. When the characteristic length Λ is large compared to unity, then diffusion due to concentration gradient dominates over creeping (diffusion due to hydrostatic pressure gradient). The coupled diffusion equation yields a time scale, which is given by

$$\tau = \frac{\Lambda^2}{D_0} = \frac{\Theta}{\dot{\epsilon}_0}. \tag{11}$$

The field quantities are normalized using the above described normalizing parameters as: spatial distance $(r, z) \rightarrow (r, z)/\Lambda$, stress $\sigma \rightarrow \sigma/\Sigma$, deviatoric stress $s \rightarrow s/\Sigma$, hydrostatic pressure $p \rightarrow p/\Sigma$, strain-rate $\dot{\epsilon} \rightarrow \dot{\epsilon}/\dot{\epsilon}_0$, velocity $v \rightarrow v\Theta/\dot{\epsilon}\Lambda$, concentration $c \rightarrow c/c_0$, time $t \rightarrow t/\tau$ and diffusivities $D's \rightarrow D's/D_0$. The weak-form of the governing differential equations (1), (6) and (7) are obtained by the application of principle of virtual work. The so-obtained weak-form was implemented in an existing finite element programme. Our formulation is completed by a constitutive relation describing the stress–strain behaviour. As mentioned earlier, we use the J_2 flow theory based power-law viscoplasticity model, which relates the deviatoric stresses and the corresponding creep strain rates as

$$s = 2\eta\dot{\epsilon}^c. \tag{12}$$

The nonlinear material parameter η in equation (12) is given by

$$\eta(\dot{\epsilon}_e) = \frac{1}{3}\dot{\epsilon}_e^{\frac{1}{n}-1}, \tag{13}$$

where $\dot{\epsilon}_e$ is the equivalent creep strain-rate. In the present study, we assume that the material power-law hardening index $n = 1$, that is a linear creep model (similar to a viscoelastic material response). In our formulation we have assumed that the elastic strain rates to be negligibly small in comparison with the creep (inelastic) strain rates. The assumption above requires the hydrostatic pressure to be treated as an independent variable and is governed by the continuity equation as described earlier. Though the hydrostatic pressure is an independent variable, it is analogous to the gradient of the particle velocity field and hence needs to be interpolated at a degree lesser than those used for the velocity field. In order to arrive at the discretized finite element form we have followed the v–p formulation similar to the u–p formulation described in Bathe (1996). In the present analysis the diffusion flux is dependent on both the concentration and the hydrostatic pressure gradients. The above implies that one needs to allow for the variation of the hydrostatic pressure in an element, which led to the choice of a 4-noded

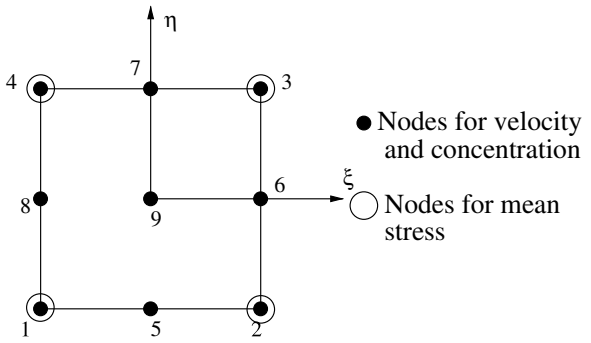

Figure 1. An isoparametric quadrilateral element used in our finite element simulations. Velocities and concentration are interpolated using a 9-noded Lagrange polynomial while the mean stress is interpolated using a 4-noded Lagrange polynomial. The matrices corresponding to the velocities and concentration are integrated using the 3×3 Gauss-quadrature integration rule, while the 2×2 integration rule is used for the hydrostatic pressure.

bi-linear Lagrange polynomial interpolation for the hydrostatic pressure. As mentioned earlier, the velocity field should be interpolated using a polynomial of a higher degree compared to the pressure field and hence was interpolated on a 9-noded, two degree of freedom per node element (figure 1). We have assumed the same 9-noded Lagrange polynomial interpolation for the concentration field. The stiffness-matrices and load-vectors corresponding to the velocity and concentration fields were obtained by using a 3×3 Gauss quadrature scheme. The matrices and vectors for the hydrostatic pressure were obtained using the 2×2 integration rule. We have used an implicit time integration scheme to update the concentration evolution at every time step. The above formulated axisymmetric coupled diffusion and creep element was implemented into an existing finite element programme. The implemented programme was used to simulate the microvoid growth problem due to selective oxidation. The details of the selective oxidation boundary value problem are presented in the next section.

3. Boundary value problem

We have simulated the selective oxidation problem analysed by Suo *et al* (2003) using the axisymmetric finite element programme described in the previous section. The schematic of the boundary value problem solved is depicted in figure 2. Following Suo *et al* (2003) we assume the continuum to be comprised of a β-NiAl alloy used as the BC in TBC. In the BC Al diffuses out and forms Al_2O_3 while Ni diffuses in the negative z direction at a rate different from that of Al diffusing out. This differential diffusion leads to an unbalanced dilatational field, that generates a large magnitude tensile stress that might nucleate a microvoid. In the present analysis, we assume the presence of such a microvoid and aim to understand the mechanics of its growth under the action of the coupled diffusion and creeping of the β-NiAl (binary alloy) in the absence of any mechanical loading. As in Suo *et al* (2003) we assume that the concentration of the point defects do not change due to straining, the amount of aluminuium diffused does not lead to any phase changes in the alloy and the elastic strain-rates are negligibly small. The axis of the microvoid shown in figure 2 is coincident with the axis of rotation z. In the present analysis we have assumed the sharpness of void as a parameter. The sharpness of the void is characterized by ψ, which is the angle made by the tangent of the void measured from the r-axis. A hemispherical void is obtained when $\psi = 90^\circ$, while the void becomes

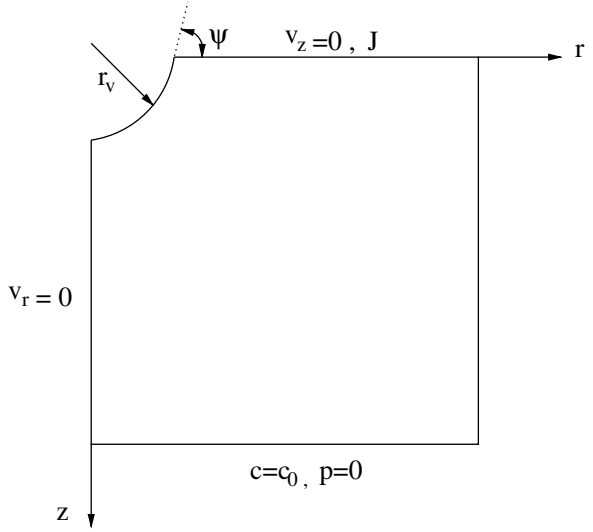

Figure 2. The geometry of the microvoid modelled in our simulations. The interface between the BC and TGO layer is represented by $z = 0$. The void is characterized by a radius r_v and angle (ψ) made between the tangent at the void corner with the interface. The diffusion flux J, which is a function of interface velocity $\dot{S}$ is applied as a Neumann boundary condition at the interface. Away from the interface a vanishing stress and flux field is assumed.

sharper for $\psi < 90^\circ$. A crack-like structure is obtained when $\psi = 0$ and is not considered here. In this work we have assumed two degrees of sharpness, they are $\psi = 90^\circ$ (hemispherical) and a sharp void with $\psi = 60^\circ$. The discretized domain is assumed to be a cylinder of radius $R = 10\,\Lambda$ and height $H = 10\,\Lambda$, with Λ being the length scale explained in equation (10). The radius of the void is assumed to be $r_v = R/8$ in our simulations. We assume that the initial composition of aluminium in the cylinder to be uniform and is set to $c(r, z, t = 0) = c_0 = 0.48$ (Suo *et al* 2003). The initial velocity and stresses are assumed to be zero at $t = \tau$. The time dependent boundary conditions are identical to those used in Suo *et al* (2003) and are given as

$$N^B(S, t) = \frac{1}{2}(1 - c_s)\sqrt{\frac{K_p}{D_o t}}, \tag{14a}$$

$$J(S, t) = -\frac{\lambda}{2}\sqrt{\frac{K_p}{D_o t}}, \tag{14b}$$

where N^B is the total atomic flux of Ni, c_s is the number fraction of Al atoms with the alloy at the interface. The position of the interface between the BC and the TGO can be written as a parabolic law:

$$S = \sqrt{\frac{K_p t}{D_o}}, \tag{15}$$

where K_p is the oxidation growth constant, which is set to $10^{-4} D_o$ (Suo *et al* 2003). In equation (14*b*), λ is a dimensional-less constant which characterizes the oxide formation. A positive value of λ denotes that new oxide layer forms at the interface of oxide and air whereas, a negative value signifies the formation of oxide at oxide–alloy interface. The concentration

at $-H$ is assumed to be invariant with time and hence we assume a zero flux condition. The above mentioned boundary conditions (equations (14*a*) and (14*b*)) have a stress singularity in time ($\sigma(t = 0) = \infty$), which is accommodated by creeping. Further growth of the microvoid is simulated by beginning our simulations at $t = \tau$ (Suo *et al* 2003). The applied boundary conditions at the interface and recession of the interface at a velocity $\dot{S}$ drives the mass transport, which leads to creeping of the material. The intrinsic diffusivities of the elements are obtained from Shankar and Siegle (1978) for the present case of β-NiAl alloy. An implicit time marching scheme is assumed for the concentration evolution equation. Using the initial concentration variation and assuming the initial velocities and stresses to be zero at $t = \tau$ the diffusion flux (J) is obtained. The diffusion flux is used to obtain the spatial variation of the velocity and stresses using the weak-form. The concentration at the next time step is obtained by using the implicit time marching till we reach the desired time in our simulation. The growth rate of the microvoid in our simulations was almost a constant after $t = 9\tau$ indicating a quasi-steady-state, which was the basis for stopping the simulations at that time step. In our formulation, we have assumed that the creeping due to the dislocation motion is anisotropic and is characterized by the parameter β_{ij}. When $\beta_{ij} = 1/3\delta_{ij}$, with δ_{ij} being the Kronecker's delta, the isotropic placement rule is obtained. In the case of isotropic placement, we assume that an atom is likely to find a sink in the form of a line dislocation with equal probabilities in all the three directions. We have performed a parametric study by varying the sharpness angle ψ and the placement rule (β) in our study. The effect of varying these parameters on the microvoid growth is described in the next section.

4. Results and discussion

In this section, we describe the results obtained from our simulations of microvoid growth due to the combined action of diffusion and creeping in a β-*NiAl* alloy. The main focus of the present study is to simulate the experimentally observed void growth pattern at the interface between the bond coat (BC) and the thermally grown oxide (TGO). In order to achieve the above said goal, we have re-simulated the selective oxidation problem solved by Suo *et al* (2003). As mentioned earlier, the above paper (Suo *et al* 2003) illustrated that a large magnitude tensile stress was generated due to the coupled diffusion and creeping driven by the selective oxidation process. In the present study, we assume that a microvoid is already present and we try to understand the mechanics of its growth due to the action of coupled diffusion and creeping of the surrounding binary alloy. The results presented in this section were obtained by varying the void sharpness and the placement rule as parameters. The void sharpness is characterized by the angle the tangent of the void makes with the r-axis (figure 2) denoted by ψ. When this angle $\psi = 90^\circ$, the void will be a hemispherical void, while the void is called a sharp void for $\psi < 90^\circ$. Following the grain boundary diffusion analysis by Needleman and Rice (1980) we have set the angle of the sharp void to be $\psi = 60^\circ$ in our analysis. The placement rule is characterized by β_{ij} described in the previous section. Creeping is isotropic when $\beta_{rr} = \beta_{\theta\theta} = \beta_{zz}$, which implies that creeping is possible with equal ease in all the three coordinate directions. In other words an atom is likely to find a sink (line dislocation) with equal probability in all the three directions. On the other hand, due to a constraint effect the creeping can become restricted in any of the directions and will be treated as a parameter in our study. We have assumed a set of β's that can predict the experimentally observed void growth trends. The effect of the void geometry on its growth can be understood by plotting the void profiles (figure 3). An isotropic placement rule is assumed in obtaining this plot. These profiles are snapshots of the void taken at regular intervals of time as the simulation progressed. Both the hemispherical and sharp voids ($\psi = 60^\circ$) simply dilate without any change in shape.

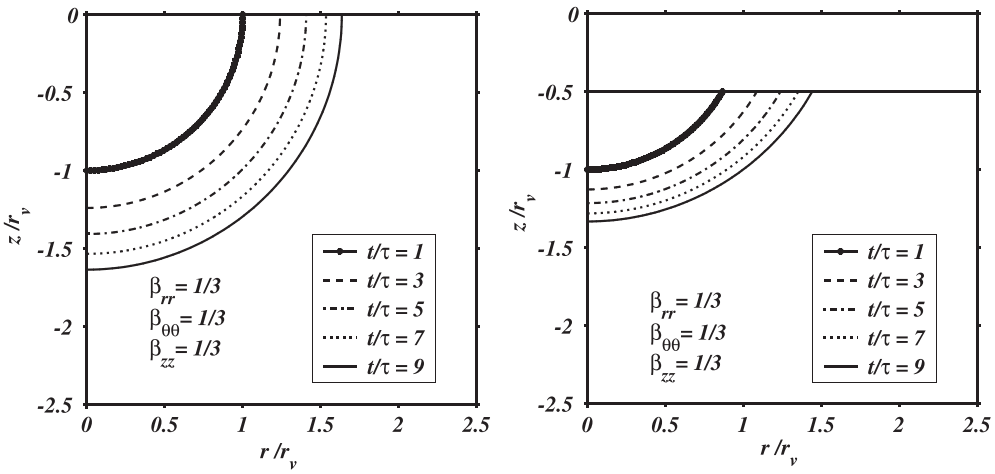

Figure 3. Snapshots of the void profiles recorded as the simulation progressed. The void profiles are normalized with the initial void radius $r_v = R/8$. The snapshots are obtained assuming an isotropic placement rule ($\beta_{rr} = \beta_{\theta\theta} = \beta_{zz} = 1/3$). For the case of isotropic placement rule the voids only dilate without any change in shape.

The hemispherical void grows faster in comparison with a sharp void, which is indicated by the larger separation distance between any two successive void profiles. This will be illustrated better by the void tip velocity history (figure 6). Isotropic creeping can occur only when the thickness of the film is sufficiently large so as to allow creeping in the z direction. As observed in the experiments by Tolpygo and Clarke (2003) a microvoid grows in the radial direction, while the growth in the thickness direction is significantly lesser. In order to mimic such a void growth pattern, we assumed a preferential placement rule by constraining the creeping to occur only in the plane (that is r–θ plane). The void growth profiles at regular intervals of time are shown in figure 4 assuming a preferential placement of $\beta_{rr} = \beta_{\theta\theta} = 1/2$ and $\beta_{zz} = 0$. The profiles are shown for both the hemispherical (left of figure 4) and sharp voids (right of figure 4). Due to the assumed preferential placement rule, the voids grow only in the plane, which is similar to the experimentally observed patterns (Tolpygo and Clarke 2003). As seen from the figure, the hemispherical void gets stretched to become an ellipsoid, while the sharp void increases in sharpness, which is characterized by a decrease in the angle ψ. In a limiting case, $\psi = 0$ represents a sharp crack. It is important to note here that the reduction in the angle ψ increases the stress concentration around the void and can lead to a stress singularity when the sharpness angle tends to zero. This transition is important in understanding the spallation failure mechanism observed in TBC systems. If the stress concentration due to the sharpness of the void is sufficiently large, the void can interact with the neighbouring voids, thereby creating a weak ligament and finally spalling (debonding) the oxide layer. In our simulations we have also assumed an orthotropic placement rule setting $\beta_{rr} = 1/3$ and $\beta_{\theta\theta} = 2/3$ with $\beta_{zz} = 0$, which resulted in a similar void growth profiles as seen with $\beta_{rr} = \beta_{\theta\theta} = 1/2$. The above mentioned orthotropic placement alters the change in sharpness of the void and void growth velocity and is discussed later in figures 5 and 6.

As seen in figures 3 and 4, the void shape change also leads to a change in the sharpness of the void. The history of the angle ψ for different placement rules is shown in figure 5. From our simulations, we see that hemispherical voids do not become sharper, that is $\psi(t) = 90^\circ \; \forall t > 0$, and hence not shown in the figure. However the sharp voids do change their sharpness with time and this is illustrated in the figure. The initial sharpness of all the voids shown in the

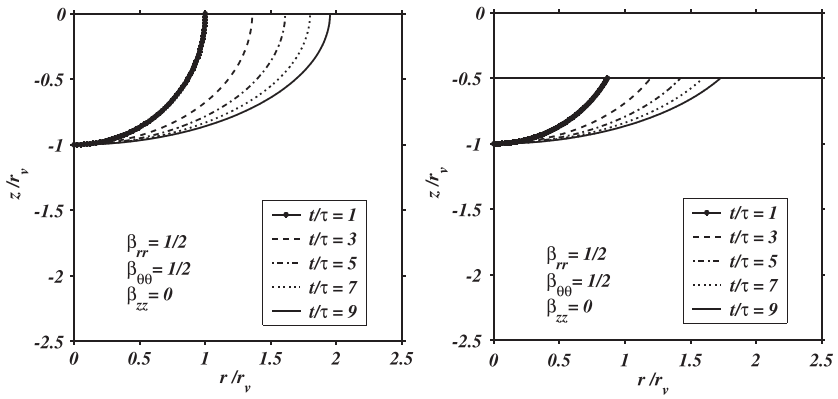

Figure 4. Snapshots of the void profiles with anisotropic placement rule. This figure is obtained by restricting the creeping to the plane by setting $\beta_{zz} = 0$. Creeping is assumed to be equally likely both in r and θ directions ($\beta_{rr} = \beta_{\theta\theta} = 1/2$). The experimentally observed pancake-shaped voids are predicted with an anisotropic placement rule as seen.

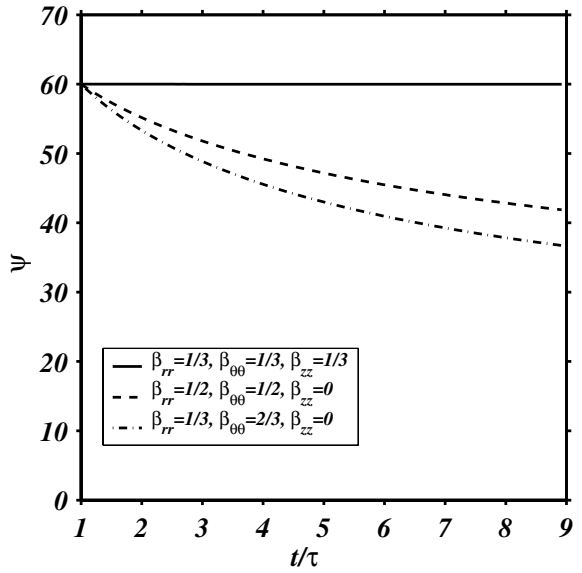

Figure 5. History of the change in sharpness of a sharp void. The sharpness remains unaffected when creeping is isotropic. The void becomes sharper (ψ decreases) for anisotropic creeping. A sharp void could progressively transform into a crack-like structure ($\rightarrow \psi = 0^\circ$).

figure is $\psi = 60^\circ$. When we assume the placement to be isotropic, then the void just dilates without any shape change indicated by the solid line that remains at 60° for any given time during our simulations. When we constrain the creep deformation to occur only in the r–θ plane, the sharpness of the void increases, indicated by the decrease in $\psi < 60^\circ$. As mentioned earlier, when we assume the creep deformation to be larger in the tangential direction, the void becomes sharper, that is the case when $\beta_{rr} = 1/3$ and $\beta_{\theta\theta} = 2/3$. When the sharpness of the void is sufficiently large the stress concentration can transform to a stress singularity leading to interactions with the neighbouring voids and hence spalling the oxide layer.

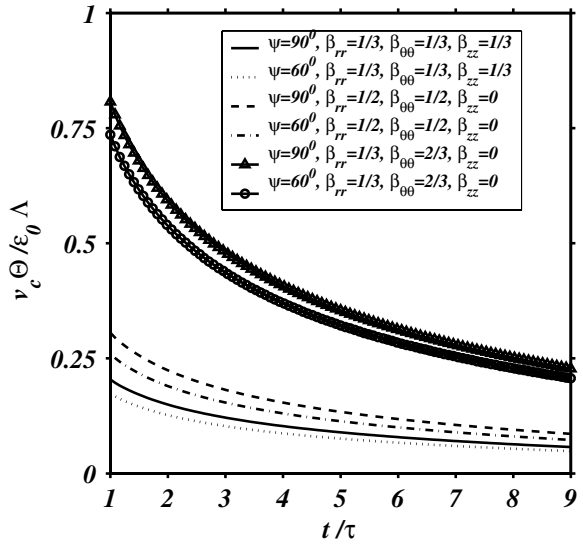

Figure 6. History of the void tip velocity for different void sharpness and placement rules. For any given placement rule a hemispherical void grows faster than a sharp void. When the creeping is restricted to the plane with $\beta_{zz} = 0$, void growth is faster compared to the case of isotropic creeping. The void growth is fastest in the case when $\beta_{rr} = 1/3$ and $\beta_{\theta\theta} = 2/3$.

The void profiles assuming isotropic and anisotropic placement rules (figures 3 and 4) showed that the distance between any two successive void profiles altered with time. This difference in the distance of separation was indicative of the change in velocity of void growth. Compared to all the points on the void, the equatorial position grows the fastest. In order to understand the effect of initial sharpness and different placement rules on the rate of change of void shape, we plot the history of the void tip velocities (figure 6). For any given placement rule, a hemispherical void grows faster compared to the sharp voids. The void tip velocity is slowest when the creep deformation is isotropic and fastest when the creep deformation is planar with creeping more likely in the tangential direction than the radial ($\beta_{\theta\theta} > \beta_{rr}$). In our study we have simulated the void growth pattern upto $t = 9\tau$, at which the change in void tip velocity almost reached a constant and hence attaining a quasi-steady-state of void growth. Even though the void growth velocity is slower in a sharp void as compared with a hemispherical void, it is important to note that the sharp void becomes sharper (figure 5) and hence leads to a magnification of the stress concentration. As mentioned earlier, a sharp void resembles the experimentally observed void shapes more closely, from which we could explain the observed spallation mechanism in the failure of TBCs.

From the results discussed so far, the effect of the sharpness of the void and placement rules on the void growth pattern were explained. In order to illustrate the effect of the presence of a void on the diffusion mechanism we plot the contours of the aluminium atom concentration in figure 7. The contours are shown for both hemispherical and sharp void shapes after the void growth reached a quasi-steady-state ($t = 9\tau$). An anisotropic placement rule described by $\beta_{rr} = 1/2$, $\beta_{\theta\theta} = 1/2$, $\beta_{zz} = 0$ was assumed, as this case closely resembles the experimentally observed void growth patterns. As mentioned earlier, we have assumed the initial concentration of Al to be $c_o = 0.48$, which is reached far away from the void. In all our simulations the Al atom diffuses out along the positive z direction into the oxide layer to form a new oxide surface. As can be seen from the contours, the shape of the void does not seem to affect the concentration

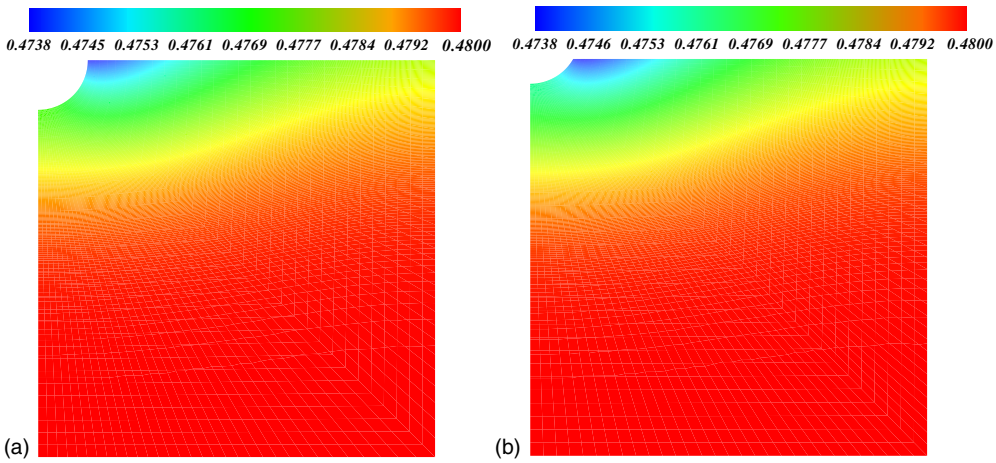

Figure 7. Aluminium atom concentration at time $t = 9\tau$. These contours were obtained with an anisotropic placement rule assuming $\beta_{rr} = 1/2$, $\beta_{\theta\theta} = 1/2$, $\beta_{zz} = 0$. The void geometry and the placement rule do not affect the variation of the concentration. The stress variations are affected by both and are illustrated in figure 8. (*a*) Hemisherical void ($\psi = 90^\circ$) and (*b*) sharp void ($\psi = 60^\circ$).

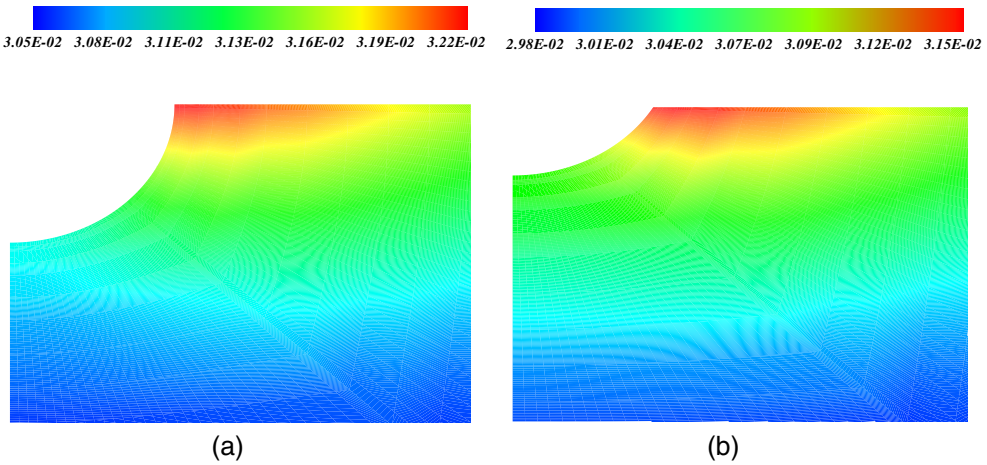

Figure 8. Radial stress (σ_{rr}/Σ) contours around the void at $t = 9\tau$. These contours are obtained assuming the same placement rule as in figure 7. The stresses are larger at the tip of the sharp void in comparison with the hemispherical void. The stress concentration around a sharp void is spread out to a larger radius indicating the effect of the void geometry. (*a*) Hemisherical void ($\psi = 90^\circ$) and (*b*) sharp void ($\psi = 60^\circ$).

distribution. The variation of the concentration is on an average a one-dimensional diffusion except close to the void as expected. It is important to note here that the mass transport occurs due to both concentration and hydrostatic pressure gradients.

The change in the concentration of Al atoms leads to a change in the stress levels and vice-versa. In order to describe the effect of the void geometry on the stresses generated, we have plotted the contours of the normalized radial stresses (σ_{rr}) in figure 8. The stress contours presented here were obtained for the same anisotropic placement rule that was used in obtaining the contours in figure 7. The stresses are plotted at $t = 9\tau$ when the simulation

predicted a quasi-steady-state. As can be seen from the contours, the stresses reach a constant homogeneous state (no variation in r or z) far away from the void. This state of stress corresponds to that obtained from a one-dimensional analysis described in Suo *et al* (2003). The magnitude of the stress increases near to the void and reaches a maximum at the tip of the void ($r = r_v$ and $z = 0$) indicated by the dark region. The effect of the microvoid geometry is more pronounced on the stress variations when compared to the concentration variations, which are indicated by a large region of inhomogeneous stress variation as opposed to a smaller area of inhomogeneous concentration variation (figure 7). Comparing the stress distribution around a hemispherical void (figure 8(a)) and a sharp void (figure 8(b)), the region of stress concentration is larger around the sharp void. This reinforces the notion that a sharp void is more critical than a hemispherical void and can lead to the experimentally observed spallation failure in TBCs.

5. Conclusions

In the present study we have extended the 1D formulation of the coupled diffusion and creeping described by Suo *et al* (2003) to the axisymmetric case. We simulated the growth of a microvoid subjected to coupled diffusion and creeping in the absence of any external mechanical loading. The simulations were performed to understand the mechanism of the void growth due to selective oxidation of β-NiAl used as a bond coat in thermal barrier coatings. We draw the following conclusions from our parametric study.

(i) The void shape remains unaffected when the creeping is assumed to be isotropic in both hemispherical and sharp voids.
(ii) Experimentally observed pancake-shaped void growth patterns occur only when creeping is suppressed (anisotropic) in the z-direction.
(iii) Maximum void growth-rate is observed in the case of hemispherical voids ($\psi = 90^\circ$) when creeping is assumed to be anisotropic.
(iv) The sharpness of a hemispherical void is independent of the placement rule. Sharp voids become sharper when the creeping is constrained to be planar and hence the stress concentration factor is magnified. In a limiting case a sharp void can transform into a crack-like ($\psi = 0^\circ$) structure, leading to interactions with the neighbouring voids and could spall the TBC as observed in experiments.

Acknowledgments

The authors would like to acknowledge the support by the Supercomputer Education Research Center (SERC) IISc, where several simulations were performed.

References

Balint D and Hutchinson J 2005 An analytical model of rumpling in thermal barrier coatings *J. Mech. Phys. Solids* **53** 949–73

Bathe K-J 1996 *Finite Element Procedure* (Englewood Cliffs, NJ: Prentice-Hall)

Brumm M and Grabke H 1993 Oxidation behavior of NiAl—II. Cavity formation beneath the oxide scale on NiAl of different stoichiometries *Corros. Sci.* **34** 547–61

Evans A, Mumm D, Hutchinson J, Meier G and Pettit F 2001 Mechanisms controlling the durability of thermal barrier coatings *Prog. Mater. Sci.* **46** 505–53

Karlsson A and Hutchinson J 2002 A fundamental model of cyclic instabilities in thermal barrier system *J. Mech. Phys. Solids* **50** 1565–89

Liu Z and Gao W 2000 Formation of interfacial voids in cast and micro-grained γ-NiAl during high temperature oxidation *Intermetallic* **8** 1385–91

Needleman A and Rice J 1980 Plastic creep flow effects in the diffusive cavitation of grain boundaries *Acta Metall.* **28** 1315–32

Provenzano V, Sadananda K, Louat N and Reed J 1988 Void formation and suppression during high temperature oxidation of MCrAlY-type coatings *Surf. Coat. Technol.* **36** 61–74

Shankar S and Siegle L 1978 Interdiffusion and intrinsic diffusion in the NiAl δ-phase of the Al–Ni system *Metall. Trans.* A **9** 1467–70

Suo Z 2004 A continuum theory that couples creep and self-diffusion ASME *J. Appl. Mech.* **71** 646–51

Suo Z, Kubair D, Evans A, Clarke D and Tolpygo V 2003 Stresses induced in alloys by selective oxidation *Acta Mater.* **51** 959–74

Svensson H, Angenete J, Stiller K and Langer V 2003 Microstructural studies of NiAl based model alloys and commercial coatings after isothermal oxidation *Mater. High Temp.* **40** 421–7

Tolpygo V and Clarke D 2000 Surface rumpling of a (ni, pt)al bond coat induced by cyclic oxidation *Acta Mater.* **48** 3283–93

Tolpygo V and Clarke D 2003 Microstructural evidence for counter-diffusion of aluminum and oxygen during the growth of alumina scale *Mater. High Temp.* **20** 261–71

Tolpygo V and Clarke D 2004a On the rumpling mechanism in nickel-aluminide coatings. part I: an experimental assessment *Acta Mater.* **52** 5115–27

Tolpygo V and Clarke D 2004b On the rumpling mechanism in nickel-aluminide coatings. part II: characterization of surface undulations and bond coat swelling *Acta Mater.* **52** 5129–41

Xu T, He M and Evans A 2003 A numerical assessment of the durability of thermal barrier system that fail by ratcheting of the thermally grown oxide *Acta Mater.* **51** 3807–20

Zimmermann D, Tolpygo V, Ruhle M and Clarke D 2003 The role of oxidation-induced cavities on the failure of the thermally grown oxide on binary beta-NiAl alloys *Z. Metallk.* **94** 157–62